Self-Resonance in Ortho-Cyclical Multi-Layer Air-Core Inductors: Analytical Techniques and Optimisation

Arun Dilip Khilnani, *Graduate Student Member, IEEE*, Lu Wan, *Member, IEEE*, Danny Roberts Seeley, *Graduate Student Member, IEEE*, Mark Sumner, *Senior Member, IEEE*, David.W.P.Thomas, *Senior Member, IEEE* and Flavia Grassi, *Senior Member, IEEE*

***Abstract*—A multi-layer air-core inductor's operational frequency limit can be known beforehand if its first self-resonance frequency can be predicted. The self-resonance frequency is due to the electrostatic capacitance stored between the turns and layers of the inductor. This paper presents an analytical technique to predict the first self-resonance frequency specifically for an ortho-cyclically wound multi-layer air-core inductor through electrostatic field segregations. The static capacitances between the inductor's turns and layers are segregated into vertical and horizontal electrostatic field components, and are further aggregated to predict the first self-resonance frequency. Further, a multi-objective optimisation technique using the pareto-optimal fronts through key parameter variations for inductor design is presented. The analytical technique is verified with acceptable results using prototype inductors. This analytical technique and optimization can be applied in designing ortho-cyclically wound multi-layer air-core inductors for low and high frequency applications.**

***Index Terms*—EMC, Self-Resonance, Static Capacitance, Air Core Inductors, Optimisation, Pareto Fronts**

NOMENCLATURE

δ_{SRF}	First SRF percentage error
$\mathrm{C}_{\mathrm{tot}}^{\mathrm{des}}$	User-defined first SRF
θ	Winding pitch angle
ε_0	Vacuum permittivity
ε_{r}	Dielectric constant of wire insulation
C_{tot}	Total static-capacitance of the inductor
C_{tt}	Turn-to-turn capacitance
$C_{\mathrm{tt}}^{\mathrm{hor}}$	Horizontal turn-to-turn capacitance
$C_{\mathrm{tt}}^{\mathrm{ver-l}}$	Vertical-left turn-to-turn capacitance
$C_{\mathrm{tt}}^{\mathrm{ver-r}}$	Vertical-right turn-to-turn capacitance
$C_{\mathrm{sum}}^{\mathrm{hor}}$	Horizontal turn-to-turn capacitance summed
$C_{\mathrm{sum}}^{\mathrm{ver-l}}$	Vertical-left turn-to-turn capacitance summed
$C_{\mathrm{sum}}^{\mathrm{ver-r}}$	Vertical-right turn-to-turn capacitance summed
d_{i}	Wire core internal diameter without insulation
d_{o}	Wire core diameter with insulation
D_{tot}	Augmenting total wire core diameter
d_{tot}	Wire core diameter with increasing layers
f_{SRF}	Inductor's first self-resonance frequency
l	Mean turn length
l_{T}	Total mean turn length
m	Number of layers
n	Number of turns-per-layer
$x(\theta_{\mathrm{hor}})$	Electrostatic Field Trace path - horizontal
$x(\theta_{\mathrm{ver-l}})$	Electrostatic Field Trace path - vertical-left
$x(\theta_{\mathrm{ver-r}})$	Electrostatic Field Trace path - vertical right

Manuscript received September 06, 2023; revised April 14, 2024

Arun Dilip Khilnani, Danny Robert Seeley, Mark Sumner and David. W. P. Thomas are with the University of Nottingham, Nottingham, The UK. (email: arun.khilnani1@nottingham.ac.uk; danny.seeley@nottingham.ac.uk; mark.sumner@nottingham.ac.uk; dave.thomas@nottingham.ac.uk)

Lu Wan is with Hitachi Energy, Baden-Daettwil, Switzerland. (email: lu.wan@hitachienergy.com)

Flavia Grassi is with Politecnico di Milano, Milan, Italy. (email: f.grassi@polimi.it)

This project research is funded by the European Union's Horizon 2020 research and innovation programme under the Marie Sklodowska-Curie grant agreement No. 812753, 812391 and 955646.

I. INTRODUCTION

AIR core inductors are passive components commonly used in power converter filters, switched-mode-power-supplies, Radio-Frequency (RF) and in Electromagnetic Compatibility (EMC) specific devices, such as the Line Impedance Stabilisation Network (LISN), owing to their low losses [1], [2]. Multi-Layer Air-Core (MLACs) are used in Radio-Frequency (RF) applications wherein a greater operation bandwidth is expected [3]. For converters operating in High Frequency (HF) range (in kHz), the filtering is usually achieved through cored inductors, that are increasingly becoming unsuitable due to inherent component limitations [4]. To augment the converter's bandwidth, MLACs could effectively be applied as effective passive components [5], [6]. In addition, given the space & volume constraints of converters following the miniaturisation trend, MLACs can provide greater inductance & operational bandwidth, if they can be geometrically designed by controlling critical parasitic components [7], [8].

The operational limit of inductors is characterised by the inherent first Self Resonance Frequency (SRF) arising from its static capacitance [9]. This static capacitance is a function of the stored electrostatic energy between the turns and windings of the inductor depending on the winding geometry [10]. If an inductor needs to be designed for a specific operational frequency limit, the electrostatic analysis of the static capacitance is critical in predicting the first SRF. To achieve this, the stored electrostatic field between the turns and windings of the MLAC inductor need to be calculated precisely. Moreover, to ensure the operational bandwidth of the application, the developed static capacitance within the inductor needs to be limited.

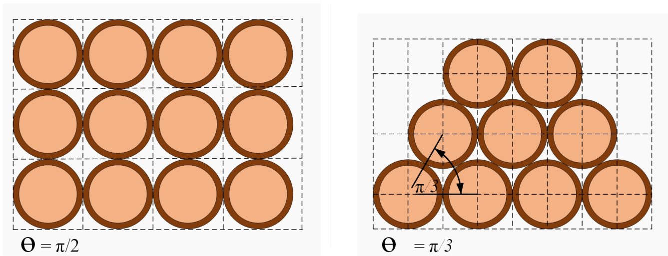

(a) Ideal Turns (b) Ortho-Cyclical Turns

Fig. 1: Winding Arrangements for MLACs

The static capacitance of single-layer inductors is described in [11], [12] through the Electrostatic Field Trace (EFT) analysis in a basic three-core cell, that represents the cross section of a two-layer ideal ortho-cyclically wound inductor. The static capacitance convergence above ten consecutive layers for a MLAC inductor is expressed as a constant function, but a layer-to-layer static capacitance development is not provided. A method for calculating the static capacitances of single-layer solenoid through an equivalent circuit is described in [13] & [14], but is not extrapolated to MLAC inductors. Similarly, [15], & [16] provide a lumped parameter approach to predict SRF, but the method becomes complex when iterated to MLAC inductors. The understanding of static capacitance modelling of inductors is explicit in [17] & [18], but with no straightforward method to predict static capacitance in MLACs.

The prediction of static capacitance for transformers is similar to that of inductors, as both are wound passive components [19]. The techniques to calculate static capacitance in transformer windings are presented in [20], [21], and are similar to those established for inductors. However, when applied to MLACs, these approaches increase the algorithmic and computational complexity involved in predicting the first SRF. Another approach for calculating the static capacitance in inductors through experimental determination by open & short circuit tests is described in [22]. This method involves a trial-&-error approach with no prior knowledge or prediction of static capacitance, and it possibly needs an empirical database of values to choose a user-specific first SRF.

Concerning design-specific optimisation, [23] describes the design procedure for a single-layer air-core inductor using sequential quadratic programming through key parameter variation. Although accurate, this method becomes tedious when applied to MLACs, as the complexity of the equations increases with the increase in EFT between the multiple layers. The design and characterisation for a single-layer air-core inductor is explained in [24], but cannot be extrapolated to MLACs as fewer key parameters are varied. Inductor optimisation using pareto-optimal fronts is described in [17], but only for cored inductors and their ac resistance, and not for the first SRF. Correspondingly, there is no simple and quick method to predict the first SRF of a MLAC inductor through an analytical technique that is accurate for EMC studies and applications.

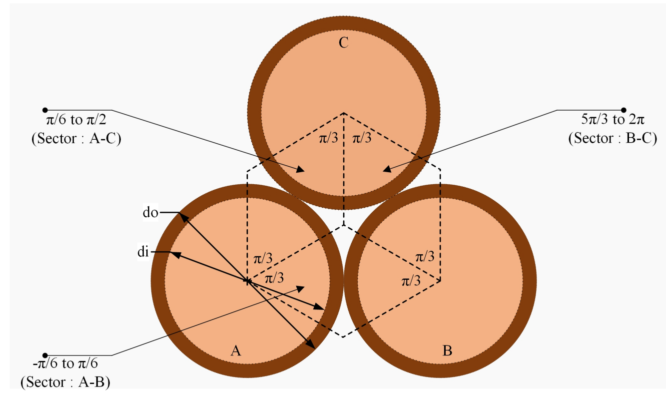

Fig. 2: Basic Cell's EFT Angles for an Ortho-Cyclical MLAC

Further, there is no optimisation procedure to establish a trade-off between the key physical parameter variations for the MLAC inductor with a specific user-defined SRF for EMC applications.

This paper presents an analytical technique for evaluating the static capacitance between physically adjacent turns in a MLAC inductor. The work presented in [11], [14] & [25] which considers an ideal ortho-cyclically wound MLAC to derive an analytical expression for predicting the first SRF of single-layer inductors is extended to MLACs (Fig.1b). The methodology involves calculating the turn-to-turn static capacitance between the turns and layers of the MLAC inductor through EFT segregation, and in formulating expressions for vertical and horizontal components. These expressions are derived in terms of the wire core diameter (d_{i}, d_{o}), number of turns per layer (n), number of layers (m) and the relative permeability of the copper's insulation coating (ϵ_{r}). Further, an optimisation technique is proposed to design a user-defined first SRF for a MLAC inductor through key physical parameter variation. The technique is a multi-objective optimization using pareto-optimal fronts applied over influential parameters of the MLAC inductor, to optimise the physical size of a MLAC inductor for a user-specified first SRF.

The remainder of the paper is organised as follows. Section II concerns the basic cell for the MLAC design and the EFT segregation between the vertical and horizontal layers. Section III derives the expression for the static capacitance in the ideal ortho-cyclically wound MLAC inductor. In Section IV, the optimization techniques for the MLAC inductor design with pareto-optimal fronts for a pre-defined SRF is described. Section V presents a COMSOL simulation to verify the validity through the basic cell. Section VI provides the experimental verification of the technique through laboratory fabricated MLAC inductor prototypes. The analytical technique is discussed in Section VII and Section VIII presents the conclusions.

II. Basic Cell Structure for the MLAC

The basic cell for the static capacitance calculation in single-layer air-core inductors is described in [11] and is applicable to ortho-cyclically wound MLAC inductors as well (Fig.1). This

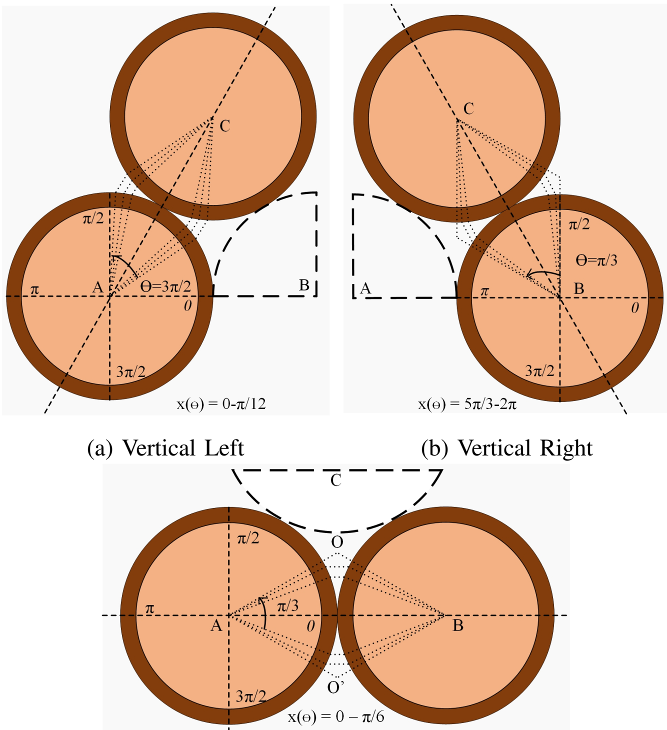

(a) Vertical Left

(b) Vertical Right

(c) Horizontal

Fig. 3: Basic Cell with Segregated EFT

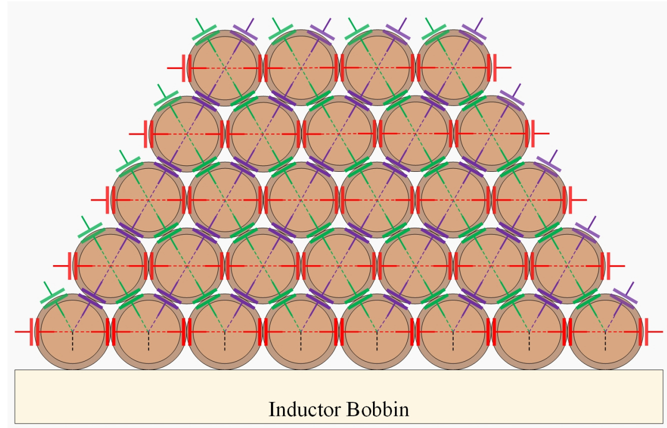

Fig. 4: Iterative Analytical Approach for the MLAC's Total Static Capacitance

basic cell is defined as a minimal and a basic turn or layer or even a macro level arrangement that represents the patterns of stored electrostatic energy between the turns (Fig.2) [25]. The turn-to-turn capacitance (C_{tt}) is derived on the assumption of a simplified EFT distribution over the basic cell, wherein the field lines are piece-wise linear and follow the shorter distance in the air-gap between turns [23]. The geometry of the inductor is influential in defining its static capacitance. An ideal MLAC inductor winding has no pitch angle (θ) (Fig. 1(a)), but practically the inductor may have an ortho-cyclical winding with a $\theta = \left(\frac{\pi}{3}\right)$, due to the winding mechanism (Fig.1(b)) [26]. This θ creates a grove-space in which the consecutive layer's wire core gets fitted creating a EFT angle. The accurate prediction of SRF for a MLAC inductor requires the C_{tt} values between the iterative conductor turns on the same layer and between the layers. It is this criterion that separates the derivation methodology for different inductor windings.

For an MLAC, the C_{tt} develops between the adjacent turns, both - horizontally and vertically. Assuming that the EFT develops consistently between the turns, the static capacitance develops at three distinct circular arc-sectors (Fig.2). In [11], this has been shown using a basic cell as well. The EFT develops at three distinct sectors along the circumference of the core, subtended at $\theta = \left(\frac{\pi}{3}\right)$ angles, that further can be segregated into three distinct components. The horizontal component ($C_{\mathrm{tt}}^{\mathrm{hor}}$) remains the same for MLAC inductors [15]. The vertical component is segregated into two distinct components: ($C_{\mathrm{tt}}^{\mathrm{ver-l}}$) and ($C_{\mathrm{tt}}^{\mathrm{ver-r}}$). Correspondingly, the three segregated static capacitances can be described as (Fig.3):

- $C_{\mathrm{tt}}^{\mathrm{hor}}$ extending from Core-A to Core-B, tracing the elementary capacitance through an angle of $\theta = \left(\frac{\pi}{3}\right)$, from the horizontal plan to a point the conductor's outer surface on the same layer of the inductor, as shown in Fig.3c [11].
- $C_{\mathrm{tt}}^{\mathrm{ver-l}}$ extending from Core-A to Core-C tracing the elementary capacitance through an angle of $\theta = \left(\frac{\pi}{3}\right)$, from the vertical plan to a point on the conductor's outer surface aligned left between two consecutive layers of the inductor, as shown in Fig.3a.
- $C_{\mathrm{tt}}^{\mathrm{ver-r}}$ extending from Core-B to Core-C tracing the elementary capacitance through an angle of $\theta = \left(\frac{\pi}{3}\right)$, from the vertical plan to a point on the conductor's outer surface aligned right between two consecutive layers of the inductor, as shown in Fig.3b.

The static capacitance for this basic cell will be a summation of these three segregated static capacitance components as observed in the cross-section (Fig.4). The analytical expressions derived for each of these components are developed using a summation approach of the MLAC's cross-sectional layout (Fig.4). The horizontal ($C_{\mathrm{tt}}^{\mathrm{hor}}$) (red) will add to ($C_{\mathrm{s}}^{\mathrm{hor}}$), as the capacitances are in series. The vertical components aligned to the left array ($C_{\mathrm{tt}}^{\mathrm{ver-l}}$) (green) and aligned to the right ($C_{\mathrm{tt}}^{\mathrm{ver-r}}$) (blue) are in series as well and will be added to obtain ($C_{\mathrm{s}}^{\mathrm{ver-l}}$) and ($C_{\mathrm{s}}^{\mathrm{ver-r}}$), respectively.

The decisive factors that affect the total value of static capacitance (C_{tot}) in MLAC inductors are :

- The dielectric constant (ϵ_{r}) of the core wire's insulating materials interposed between the conductor layers,
- The inductor's geometry and physical size (D_{tot}, d_{tot}, m, n),
- The wire core's insulation thickness (d_{o}),
- The winding technique and the pitch angle (θ) and,
- The inter & the outer diameter of the MLAC inductor (d_{i}, d_{o})

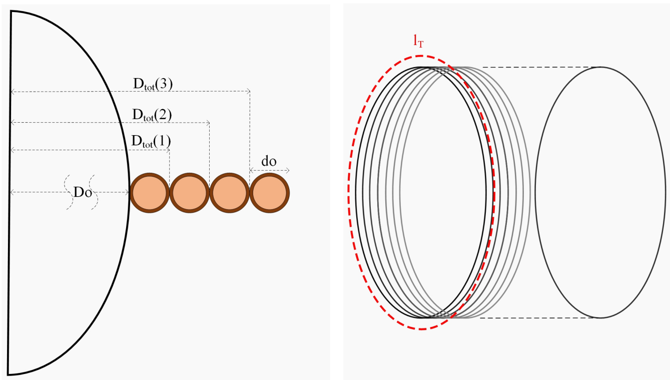

(a) Increasing Total Diameter (b) Mean Turn Lengths

Fig. 5: Increasing Diameter with Layers

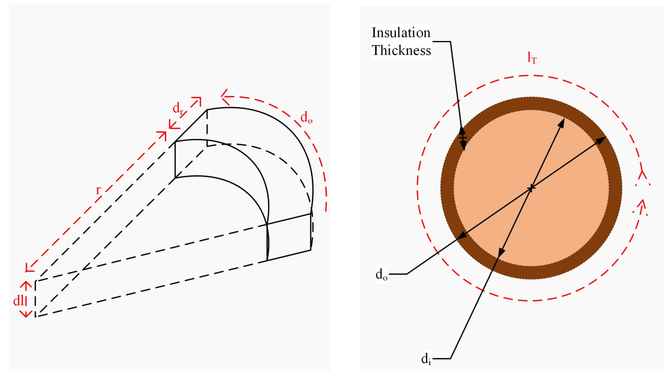

(a) Elementary Surfaces (b) Wire Core's Diameters

Fig. 6: Elementary Surface Turn-to-Turn Capacitance

III. Analytical Expression for MLAC

The basic cell configuration for the MLAC inductor consists of two adjacent round conductors of the same layer (A & B), along with one round conductor turn (C) forming the first layer (Fig.2 & 3). This basic cell can be considered as a basic building block for the complete MLAC inductor for the vertical and horizontal arrays of such building blocks.

The center-point in the air-gap between the turns, wherein the wire cores physically touch, can be considered as the origin of the EFT axis (Fig.2 & 3). The distance $x(\theta)$ is the shortest EFT-path on the horizontal and vertical axis that extends for $\theta = \left(\frac{\pi}{3}\right)$ [11]. For the MLAC inductor, this EFT path develops at three distinct sectors on the outer circumference of the wire conductor (Fig.3). The analytical expression for (C_{tot}) can then be derived through the summations of ($C_{\mathrm{sum}}^{\mathrm{hor}}$), ($C_{\mathrm{sum}}^{\mathrm{ver-l}}$ and ($C_{\mathrm{sum}}^{\mathrm{ver-r}}$). To derive these analytical expressions, the following assumptions are made:

- The winding type for the MLAC inductor is an ideal case of the ortho-cyclical winding, with a perfect pitch angle of $\left(\frac{\pi}{3}\right)$ (Fig. 1b).
- The electrostatic field is assumed to be static and the incremental increase in capacitances across all three segregations due to the dynamic changes in the EFT is neglected.
- The fringe EFTs that may surround the inductor are neglected.
- The voltage distribution at every consecutive turn within a layer and between the layers is uniform, with equal magnetic flux linkage that develops the inductance.
- The total mean turn length (l_{T}) remains consistent for every turn through the layer and increases by the inductor wire diameter (d_{o}) to (D_{tot}) at every consecutive layer (Fig.5b). The distance of every consecutive layer from the center-point also increases by d_{o} (Fig.5a).

Correspondingly, the elementary capacitance (dC) of a single-core of the inductor can generally be expressed as [11]:

$$dC = \frac{\epsilon_{\mathrm{r}}}{dr} d\theta dl \tag{1}$$

wherein:

- $\epsilon = \epsilon_0 \epsilon_{\mathrm{r}}$, where $\epsilon_0 = 8.854e^{-12}\mathrm{F/m}$ is the absolute permittivity of the free space. The ϵ_{r} is an important parameter as it can affect the C_{tt} and further change the cumulative C_{tot} for the MLAC inductor, significantly affecting its SRF.
- $d\theta$ is sectoral radius that encompasses the electrostatic-field trace (Fig.6a).
- dl is the sectoral circumference that the EFT (Fig.6b).

In (1), the length (l) of each inductor turn is of finite length (Fig.5a). The elementary capacitance of the wire conductor's insulation coating (dC_{c}) due to the elementary surface (subtended by θ for the wire conductor's radius) from (r_{i}) to (r_{o}) and the length (l) from zero to the one mean turn length (l_{T}) is expressed as :

$$dC_{\mathrm{c}} = \epsilon_0 \epsilon_{\mathrm{r}} \theta \int_0^{l_{\mathrm{T}}} dl \int_{r_{\mathrm{i}}}^{r_{\mathrm{o}}} \frac{r}{dr} = \frac{\epsilon l_{\mathrm{T}}}{2\ln\left(\frac{d_{\mathrm{o}}}{d_{\mathrm{i}}}\right)} d\theta \tag{2}$$

As there is negligible spacing between the horizontal and vertical turns of the MLAC inductor within the air-gap (Fig.2 & Fig.4), the total distance then between the two adjacent turns can then be traced as :

- $x(\theta_{\mathrm{hor}})$ for $C_{\mathrm{tt}}^{\mathrm{hor}}$, as seen in Fig.3(c),
- $x(\theta_{\mathrm{ver-l}})$ for $C_{\mathrm{tt}}^{\mathrm{ver-l}}$, as seen in Fig.3(a) and,
- $x(\theta_{\mathrm{ver-r}})$ for $C_{\mathrm{tt}}^{\mathrm{ver-r}}$, as seen in Fig.3(b).

The elementary capacitance developed due to the wire conductor's insulation coatings of the two adjacent turns connected in series will be the same for all the three segregated static capacitances. This elementary capacitance (dC_{ttc}) can be expressed as:

$$dC_{\mathrm{ttc}} = \frac{dC_{\mathrm{c}}}{2} = \frac{\epsilon l_{\mathrm{T}}}{2\ln(\frac{r_{\mathrm{o}}}{r_{\mathrm{i}}})} d\theta = \frac{\epsilon l_{\mathrm{T}}}{2\ln(\frac{d_{\mathrm{o}}}{d_{\mathrm{i}}})} d\theta \tag{3}$$

This static capacitance develops at three different angles for each of the segregations [$x(\theta_{\mathrm{hor}})$, $x(\theta_{\mathrm{ver-l}})$ & $x(\theta_{\mathrm{ver-r}})$], and can be commonly expressed as:

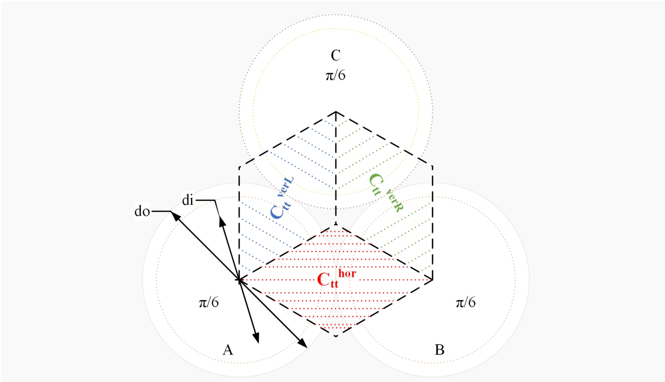

Fig. 7: Elementary Surfaces Segregated for the Basic Cell

$$\cos(\theta) = \left(\frac{\dfrac{d_0}{2} - \dfrac{x(\theta)}{2}}{\dfrac{d_0}{2}} \right) \tag{4}$$

which becomes,

$$x(\theta) = d_{\mathrm{o}}(1 - \cos(\theta)) \tag{5}$$

The elementary surface (dS) of the conductor wire including the insulation coating for the turn length (l_{T}) is :

$$dS = \frac{d_{\mathrm{o}} l_{\mathrm{T}}}{2} d\theta \tag{6}$$

Therefore, as per the basic cell the elementary capacitance due to the air-gap between the two turns can be expressed for the three segregations [$dC_{\mathrm{g}}^{\mathrm{hor}}$, $dC_{\mathrm{g}}^{\mathrm{ver-l}}$, $dC_{\mathrm{g}}^{\mathrm{ver-r}}$], and can be commonly written as (dC_{g}) :

$$dC_{\mathrm{g}} = \frac{\epsilon_o dS}{x(\theta)} \tag{7}$$

which becomes,

$$dC_{\mathrm{g}} = \frac{\epsilon_o l_T}{2d_o(1 - \cos(\theta))} \tag{8}$$

For turns with no spacing between them, the elementary capacitance due to the insulation coating is much higher than the air-gap capacitance [11], [14]. Generally, the series combination of the elementary capacitances of the air-gap between the two adjacent turns and the insulating coating of the two adjacent turns is given by:

$$dC_{\mathrm{tt}}(\theta) = \left(\frac{dC_{\mathrm{tt}} dC_{\mathrm{g}}}{dC_{\mathrm{tt}} + dC_{\mathrm{g}}} \right) \tag{9}$$

By substituting (8) in (9), this series combination for the three segregations [$dC_{\mathrm{tt}}(\theta)^{\mathrm{hor}}$,$dC_{\mathrm{tt}}(\theta)^{\mathrm{ver-l}}$, $dC_{\mathrm{tt}}(\theta)^{\mathrm{ver-r}}$] can be commonly expressed as [$dC_{\mathrm{tt}}(\theta)$]:

$$dC_{\mathrm{tt}}(\theta) = \frac{\varepsilon_0 l_{\mathrm{T}}}{2\left[\dfrac{1}{\epsilon_{\mathrm{r}}} \ln(\dfrac{d_{\mathrm{o}}}{d_{\mathrm{i}}}) + 1 - \cos(\theta) \right]} \tag{10}$$

The EFT is different for all three segregations and the three angles can be traced based on the frames of reference as per the basic cell. These angles can be traced as :

- For ($C_{\mathrm{tt}}^{\mathrm{hor}}$), the $x(\theta_{\mathrm{hor}})$ traces from $\theta = \left(-\dfrac{\pi}{6}\right)$ to $\theta = \left(\dfrac{\pi}{6}\right)$ for a total of $\theta = \left(\dfrac{\pi}{3}\right)$ as explained in [11] (Fig.7),
- For ($C_{\mathrm{tt}}^{\mathrm{ver-l}}$), the $x(\theta_{\mathrm{ver-l}})$ traces from $\theta = \left(\dfrac{\pi}{6}\right)$ to $\theta = \left(\dfrac{\pi}{2}\right)$ for a total of $\theta = \left(\dfrac{\pi}{3}\right)$, with Core A as the frame of reference (Fig.7),
- For ($C_{\mathrm{tt}}^{\mathrm{ver-r}}$), the $x(\theta_{\mathrm{ver-r}})$ traces from $\theta = \left(\dfrac{5\pi}{3}\right)$ to $\theta = (2\pi)$ for a total of $\theta = \left(\dfrac{\pi}{3}\right)$, with the core B as the reference frame (Fig.7).

Correspondingly, these limits of integration are applied to (10) using the following integral [14],

$$\int \frac{dx}{a - \cos x} = \frac{2}{\sqrt{a^2 - 1}} \arctan\left[\sqrt{\frac{a+1}{a-1}} \tan\frac{x}{2} \right] \tag{11}$$

For the horizontal trace,

$$C_{\mathrm{tt}}(\theta_{\mathrm{hor}}) = \int_{-\frac{\pi}{6}}^{\frac{\pi}{6}} \frac{\varepsilon_0 l_{\mathrm{T}}}{2\left[\dfrac{1}{\epsilon_{\mathrm{r}}} \ln(\dfrac{d_{\mathrm{o}}}{d_{\mathrm{i}}}) + 1 - \cos(\theta_{\mathrm{hor}}) \right]} \tag{12}$$

and rearranges to (15).

For the vertical left trace,

$$C_{\mathrm{tt}}(\theta_{\mathrm{ver-l}}) = \int_{\frac{\pi}{12}}^{\frac{\pi}{2}} \frac{\varepsilon_0 l_{\mathrm{T}}}{2\left[\dfrac{1}{\epsilon_{\mathrm{r}}} \ln(\dfrac{d_{\mathrm{o}}}{d_{\mathrm{i}}}) + 1 - \cos(\theta_{\mathrm{ver-l}}) \right]} \tag{13}$$

and rearranges to (16).

For the vertical right trace,

$$C_{\mathrm{tt}}(\theta_{\mathrm{ver-r}}) = \int_{\frac{5\pi}{3}}^{2\pi} \frac{\varepsilon_0 l_{\mathrm{T}}}{2\left[\dfrac{1}{\epsilon_{\mathrm{r}}} \ln(\dfrac{d_{\mathrm{o}}}{d_{\mathrm{i}}}) + 1 - \cos(\theta_{\mathrm{ver-r}}) \right]} \tag{14}$$

and rearranges to (17).

The MLAC inductor's diameter increases with the addition of every layer through the wire inductor's diameter (Fig.5a). To accurately develop the analytical formulae, this is factored in the expressions developed (16), (17) & (12). When a transverse cross section of the MLAC inductor is considered, the horizontal summation ($C_{\mathrm{s}}^{\mathrm{hor}}$) will be in a series combination of ($C_{\mathrm{tt}}^{\mathrm{hor}}$) developed at every turn in the MLAC inductor, as the EFT will be bifurcated from that perspective. This will be further multiplied by the total layers (Fig.4). The summation then can be expressed as [11]:

$$C_{\mathrm{tt}}^{\mathrm{hor}}=\frac{2\epsilon_0\pi D_{\mathrm{o}}}{\sqrt{\left(\frac{2}{\epsilon_{\mathrm{r}}}\right)\ln\left(\frac{D_{\mathrm{tot}}}{d_{\mathrm{i}}}\right)\left(1+\frac{1}{\epsilon_{\mathrm{r}}}\right)}}\left\{\arctan\left[\frac{1}{\sqrt{3}}\sqrt{\frac{2+\left(\frac{1}{\epsilon_{\mathrm{r}}}\right)\ln\left(\frac{D_{\mathrm{tot}}}{d_{\mathrm{i}}}\right)}{\left(\frac{1}{\epsilon_{\mathrm{r}}}\right)\ln\left(\frac{D_{\mathrm{tot}}}{d_{\mathrm{i}}}\right)}}\right]\right\} \tag{15}$$

$$C_{\mathrm{tt}}^{\mathrm{ver-l}}=\frac{2\epsilon_0\pi D_{\mathrm{o}}}{\sqrt{\left(\frac{2}{\epsilon_{\mathrm{r}}}\right)\ln\left(\frac{D_{\mathrm{tot}}}{d_{\mathrm{i}}}\right)\left(1+\frac{1}{\epsilon_{\mathrm{r}}}\right)}}\left\{\arctan\left[\frac{2}{\sqrt{3}+3}\sqrt{\frac{2+\left(\frac{1}{\epsilon_{\mathrm{r}}}\right)\ln\left(\frac{D_{\mathrm{tot}}}{d_{\mathrm{i}}}\right)}{\left(\frac{1}{\epsilon_{\mathrm{r}}}\right)\ln\left(\frac{D_{\mathrm{tot}}}{d_{\mathrm{i}}}\right)}}\right]\right\} \tag{16}$$

$$C_{\mathrm{tt}}^{\mathrm{ver-r}}=\frac{2\epsilon_0\pi D_{\mathrm{o}}}{\sqrt{\left(\frac{2}{\epsilon_{\mathrm{r}}}\right)\ln\left(\frac{D_{\mathrm{tot}}}{d_{\mathrm{i}}}\right)\left(1+\frac{1}{\epsilon_{\mathrm{r}}}\right)}}\left\{\arctan\left[\frac{2}{\sqrt{3}-1}\sqrt{\frac{2+\left(\frac{1}{\epsilon_{\mathrm{r}}}\right)\ln\left(\frac{D_{\mathrm{tot}}}{d_{\mathrm{i}}}\right)}{\left(\frac{1}{\epsilon_{\mathrm{r}}}\right)\ln\left(\frac{D_{\mathrm{tot}}}{d_{\mathrm{i}}}\right)}}\right]\right\} \tag{17}$$

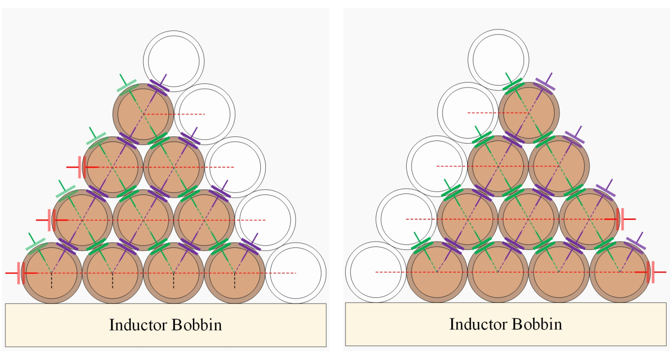

(a) Vertical Right Array Residues (b) Vertical Left Array Residues

Fig. 8: Tapering-ends Residual Capacitances

$$C_{\mathrm{s}}^{\mathrm{hor}}=\sum_{\mathrm{m}}^{\mathrm{m.do+D_{tot}}}\frac{C_{\mathrm{tt}}^{\mathrm{hor}}}{n-1}m \tag{18}$$

Correspondingly, the vertical-left array ($C_{\mathrm{s}}^{\mathrm{ver-l}}$) and the vertical-right array ($C_{\mathrm{s}}^{\mathrm{ver-r}}$) summations will be a series combinations of ($C_{\mathrm{tt}}^{\mathrm{ver-l}}$) and ($C_{\mathrm{tt}}^{\mathrm{ver-r}}$), respectively on every layer (Fig.4). These will be further multiplied by the total turns-per-layer. The summations can be expressed as :

$$C_{\mathrm{s}}^{\mathrm{ver-l}}=\sum_{\mathrm{m}}^{\mathrm{m.do+D_{tot}}}\frac{C_{\mathrm{tt}}^{\mathrm{ver-l}}}{m-1}n \tag{19}$$

$$C_{\mathrm{s}}^{\mathrm{ver-r}}=\sum_{\mathrm{m}}^{\mathrm{m.do+D_{tot}}}\frac{C_{\mathrm{tt}}^{\mathrm{ver-r}}}{m-1}n \tag{20}$$

The summation for the ($C_{\mathrm{s}}^{\mathrm{ver-l}}$) and ($C_{\mathrm{s}}^{\mathrm{ver-r}}$) is incomplete due to the inherent limitations offered by the analytical technique. The summations do not account for ($C_{\mathrm{tt}}^{\mathrm{ver-r}}$) and ($C_{\mathrm{tt}}^{\mathrm{ver-l}}$) that exist over the tapering end of the MLAC inductor formed due to the ortho-cyclical winding (Fig.8). These residual capacitances need to be included and can be expressed as:

$$C_{\mathrm{sum}}^{\mathrm{res}}=\sum_{\mathrm{q=1}}^{\mathrm{m-1}}C_{\mathrm{tt}}^{\mathrm{ver-l}}(n-m+1)+\sum_{\mathrm{p=1}}^{\mathrm{m-1-k}}C_{\mathrm{tt}}^{\mathrm{ver-l}} \tag{21}$$

wherein, q is the horizontal residue static capacitance component and p is for both the vertical components. The integer k represents the wire core's capacitance excluded due to the summation technique in Fig.4, but is now considered.

Correspondingly, the total static capacitance can be expressed as :

$$C_{\mathrm{tot}}=C_{\mathrm{s}}^{\mathrm{hor}}+C_{\mathrm{s}}^{\mathrm{ver-l}}+C_{\mathrm{s}}^{\mathrm{ver-r}}+C_{\mathrm{sum}}^{\mathrm{res}} \tag{22}$$

Finally, the first self-resonance frequency (f_{SRF}) for the inductor with inductance (L) is,

$$f_{\mathrm{SRF}}=\frac{1}{2\pi\sqrt{LC_{\mathrm{tot}}}} \tag{23}$$

IV. Simulations

To verify the assumptions about the EFT integration angles that were considered for ($C_{\mathrm{tt}}^{\mathrm{ver-l}}$) and ($C_{\mathrm{tt}}^{\mathrm{ver-r}}$) to derive the analytical formulas in (15), (16) and (17), a simulation in COMSOL Multiphysics™ was performed. The assumptions for the EFT in [11], [21] & [27] to verify the angles for the ($C_{\mathrm{tt}}^{\mathrm{hor}}$) was extended to the ($C_{\mathrm{tt}}^{\mathrm{ver-l}}$) and ($C_{\mathrm{tt}}^{\mathrm{ver-r}}$), to partly validate the formulas in (16), (17) and (12). The horizontal EFT is validated to extend for $x(\theta)=\left(\frac{\pi}{3}\right)$, from $\left(-\frac{\pi}{6}\right)$ to $\left(\frac{\pi}{6}\right)$ in [11]. However, the vertical EFT field traces are yet to be validated to confirm if they indeed extend for $x(\theta)=\left(\frac{\pi}{3}\right)$ for the ($C_{\mathrm{tt}}^{\mathrm{ver-l}}$) and ($C_{\mathrm{tt}}^{\mathrm{ver-r}}$) components respectively.

As per [11], the air-gap capacitance beyond $\left(\frac{\pi}{3}\right)$ is negligible and that fringe EFT is negligible as well. To validate

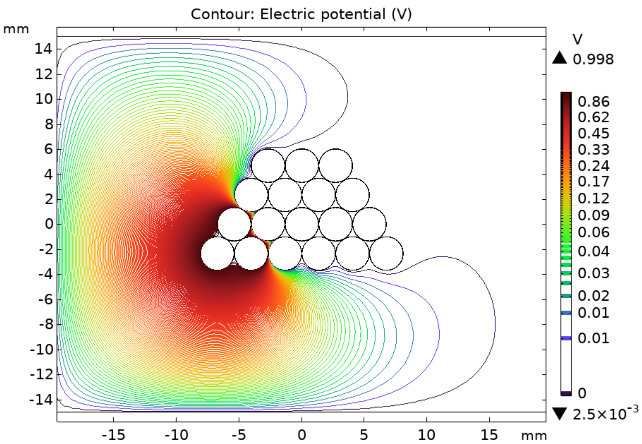

Fig. 9: Electric Field Trace in the Basic Cell

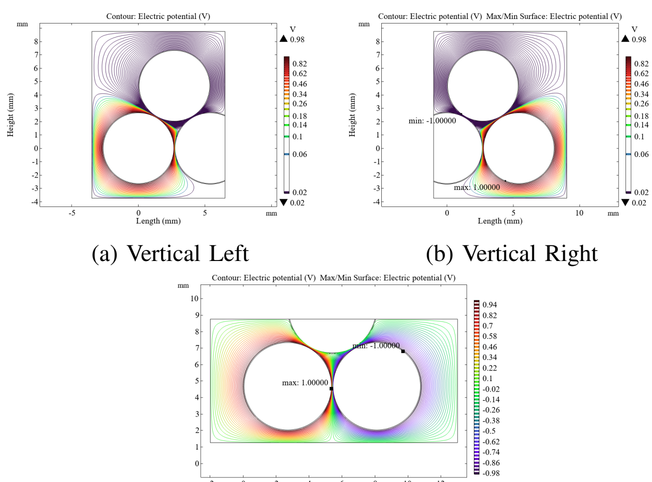

(a) Vertical Left

(b) Vertical Right

(c) Horizontal

Fig. 10: Basic Cell with Segregated EFT in Simulation

this assumption, the 2D stationary simulation for an ortho-cyclically wound MLAC with sufficient turns was made, with the basic cell in Fig.2 excited by a unit voltage while the other wire cores were held at zero potential (Fig.9). The EFT gradient's influence was not seen beyond the basic cell, while the adjacent wire cores seemed to have negligible influence. The maximum ($+1$ V/mm) and the minimum values ($6.25e^{-3}$ V/mm,) of the distributed electric field proved that the fringe effect between adjacent cores was negligible. This proved that although not zero, the fringe EFT was not influential and can be deemed relatively insignificant in the analytical formulation.

To validate EFT angles assumptions for integration, a 2D stationary simulation for each segregated EFT (3) was created. The cores were energized with unit positive and negative voltages (Fig.10). The EFT lines were then tested for point-evaluations from 0 to $\left(\frac{\pi}{3}\right)$ in steps of $\left(\frac{\pi}{18}\right)$, (i.e, every 5°).

A. Vertical-left EFT

To verify the EFT angles of integration for the ($C_{\text{tt}}^{\text{ver}-\text{l}}$), the core A was excited with a unit positive voltage, while core C was excited with a unit negative voltage to create a polarity, and the core B was held at ground potential (Fig.10a).

B. Vertical-right EFT

To verify the EFT angles of integration for the ($C_{\text{tt}}^{\text{ver}-\text{r}}$), the core B was excited with a unit positive voltage, while core C was excited with a unit negative voltage to create a polarity, and the core A was held at ground potential (Fig.10b).

C. Horizontal EFT

To verify the EFT angles of integration for the ($C_{\text{tt}}^{\text{hor}}$), the core A was excited with a unit positive voltage, while core B was excited with a unit negative voltage to create a polarity, and the core C was held at ground potential (Fig.10c).

Hence, the EFT angles of integration for the ($C_{\text{tt}}^{\text{ver}-\text{l}}$), ($C_{\text{tt}}^{\text{ver}-\text{r}}$) and ($C_{\text{tt}}^{\text{hor}}$) are justified to be limited between 0 to $\left(\frac{\pi}{3}\right)$, as the EFT value drops rapidly between $\left(\frac{\pi}{6}\right)$ to $\left(\frac{\pi}{4}\right)$ (Fig.9). The simulations results here were limited by the boundary limits set in this case, but the decrease in the EFT value remains consistent and can be considered in good agreement with the hypothesis proposed in [15].

V. Experimental Set-up and Results

Equations (15), (16), (17) and (18)-(23) were applied to obtain the first SRF for every MLAC inductor. The inductance (expressed in mH) of the MLAC was obtained using the Wheeler's formula (24). To verify the analytical expressions, four laboratory based inductor prototypes were fabricated an an inductor bobbin (Fig.11a). To show the effectiveness and the shortcomings of the proposed analytical method, the first four fabricated MLAC inductors (A,B,C & D) were chosen to have the same diameter. In doing so, the consecutive increase in the C_{tot} and the increasing δ_{SRF} was observed. The final inductor was chosen with a greater D_{tot} and and with a smaller d_{o} to show the increase in δ_{SRF}. Their first SRF was measured using the Keysight™E4990A impedance analyser in the frequency range 20 Hz to 120 MHz (Fig. 11b). The percentage error between the measured and analytical SRF were calculated using (25) :

$$\mathrm{L(mH)} = \frac{31.6n^2\left(\frac{D_{\text{tot}}}{2}\right)}{6\left(\frac{D_{\text{tot}}}{2}\right) + 9l + 10(r_2 - r_1)} \tag{24}$$

$$\delta_{SRF} = \frac{(f_{\text{srf}}^{\text{meas.}} - f_{\text{srf}}^{\text{analy.}})}{f_{\text{srf}}^{\text{meas.}}}(100) \tag{25}$$

The measurement results are tabulated in Table.(I). To verify the analytical expressions, different D_{tot}, m and n were applied, along with different wire core diameters. It was

TABLE I: Comparisons between the measured and the analytical SRF for inductor prototypes

L (mH)	D_{tot} (mm)	d_{i} (mm)	d_{o} (mm)	m	n	$C_{\text{tot}}^{\text{calc}}$ (nF)			f_{calc} (kHz)			$C_{\text{tot}}^{\text{meas}}$ (nF)	f_{meas} (kHz)	δ_{SRF}
						ϵ_{r}			ϵ_{r}					
						2.8	***3.78***	4.5	2.8	***3.78***	4.5	$\epsilon_r = 3.78$	$\epsilon_r = 3.78$	$\epsilon_r = 3.78$
0.619 (A)	100	2.65	2.7	48-47	2	0.819	**1.019**	1.151	223.50	**200.31**	188.54	**1.153**	**188.36**	**-6.34**
1.34 (B)	100	2.65	2.7	48-47-46	3	0.819	**1.019**	1.151	151.91	**136.14**	128.17	**0.852**	**148.95**	**8.56**
2.285 (C)	100	2.65	2.7	48 to 45	4	0.626	**0.779**	0.919	133.03	**119.21**	112.23	**2.72**	**122.55**	**2.3**
3.43 (D)	100	2.65	2.7	48 to 44	5	0.678	**0.707**	0.798	114.06	**102.20**	96.22	**0.706**	**96.973**	**-5.40**
2.360 (E)	150	1.25	1.35	22 to 18	5	0.116	**0.146**	0.165	309.88	**276.81**	260.12	**0.205**	**233.03**	**15.8**

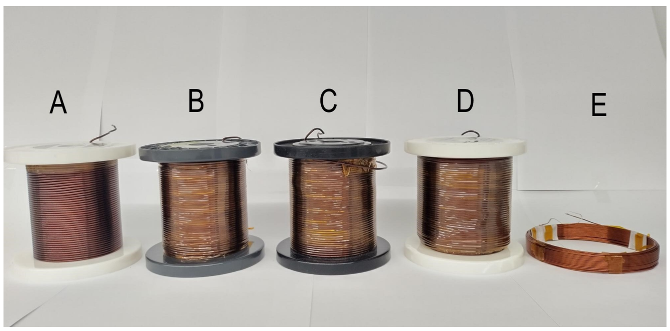

(a) InductorPrototypes

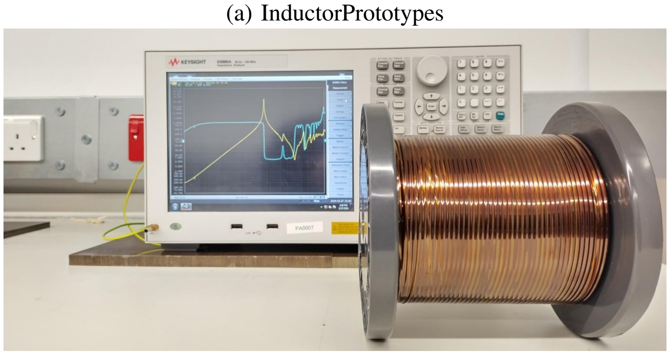

(b) Measurement Setup

Fig. 11: Inductor prototypes and measurement setup

observed that the percentage error increased as the layers were increased, indicating that the ortho-cyclical winding turns becomes wild-winding as the turns increase. The influence of insulation permittivity (ϵ_{r}) for the wire core's insulation was noticed. To the best of the author's knowledge, the ϵ_{r} for the poly-amide insulation varies between (ϵ_{r})=2.8 to 4.5. Since different wire core diameters will have different insulation thickness, an average value of $\epsilon_{\text{r}} = 3.78$ was applied. As per the tabulated results, the influence of ϵ_{r} can be seen with the δ_{SRF} having lower error for $\epsilon_{\text{r}} = 2.8$ and progressively increase to $\epsilon_{\text{r}} = 4.5$. Hence, the poly-amide insulation seems to be a sensitive parameters influencing the first SRF of the MLAC inductor. Hence, to elongate the frequency range of the inductors, a lower value can be advantageous.

An impedance co-relation graph was then considered between the calculated and the measured impedances of the considered inductor prototypes. The calculated impedance was derived using the inductance calculated from Wheeler's formula (24), static capacitance from the derived expressions in (15), (16) & (17), while the resistance was considered from the actual measurement of the prototypes. The Keysight™E4990A impedance analyser was then applied to measure the impedance of the inductor prototypes. The results for the inductor prototype C showed a decent discrepancy between the calculated and the measured impedances (Fig. 12). For all the five considered prototypes, an impedance mismatch was observed between the calculated and measured impedances. This highlighted the need to consider the influence of resistance of the wire core in determining the actual impedance, along with the first SRF prediction. Further influences are described in Section VII.

VI. Optimisation Technique

The formulae for the segregated static capacitances of the MLAC inductor can be applied to optimise the MLAC inductor. This optimisation can be for a user-defined first SRF in minimising the physical dimensions of the MLAC inductor. In most converters and EMC based applications, the inductance is fixed along with the wire-conductor's thickness to maintain the required current. The type of the inductor (air-core or ferrite-core) is usually pre-decided, while the space requirements depend on the type of the application. Correspondingly, the key parameters that influence the first SRF are:

- Total static capacitance (C_{tot})
- Inductance (L)
- Internal diameter/radius of the inductor ($d_{\text{o}} \mid r_{\text{o}}$)
- Turns per Layer (n)
- Layers (m)
- Thickness of Wire conductor (d_{i}) and
- Relative Permittivity of the Conductor (ϵ_{o}).

To augment the operational frequency of the MLAC inductor with a fixed diameter, the inductor length (governed by the turns-per-layer) and the total breath (governed by the turns-per-layer and the bobbin diameter) can be influenced. A Multi-Objective Optimisation technique using Pareto Optimal Fronts (POF) can then be applied to obtain optimal solutions for these parametric variations [6], [28], [29]. By applying a POF to the optimisation, a range of feasible solutions for the MLAC inductor can be obtained. These feasible solutions can provide multiple choices for the MLAC inductor design for different set of variables and constraints [18]. The POF provides a set of non-dominated solutions, where each objective is considered to be equally good.

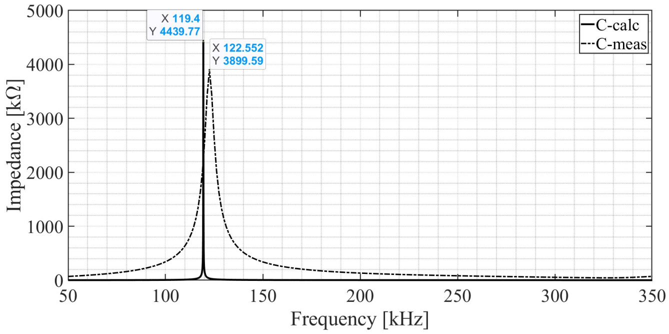

Fig. 12: Impedance Co-relation for the Prototype Inductor C

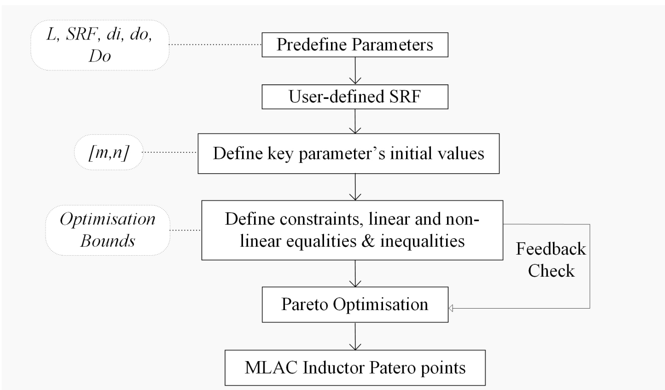

Fig. 13: Patero Optimisation Algorithm

In design problems, a single-objective optimisation of a function $[f(x)]$ is considered, but for multi-objective optimisation, there is a requirement for multiple functions $[f_n(x)]$:

$$f(x) = [f_1(x), f_2(x), f_3(x), f_4(x) \cdots f_n(x)]^{\mathrm{T}} \tag{26}$$

To obtain feasible solutions, the constraints applied over the functions for optimisation can be defined as :

$$g_{\mathrm{j(x)}} \geq 0|j| = 1, 2, 3, 4 \cdots \tag{27}$$

$$h_{\mathrm{k(x)}} \geq 0|k| = 1, 2, 3, 4 \cdots \tag{28}$$

The constraints $[g_{\mathrm{j(x)}}]$ & $[h_{\mathrm{k(x)}}]$ are defined over $[f(x)]$ and can be linear or non-linear as well. To maintain the feasibility of the optimal solutions, upper and lower bounds are applied to the optimisation process.

To apply the pareto-optimisation process to the MLAC inductor, the objectives are (Fig.13) :

- To reduce the length of the MLAC inductor, minimise n through $C_{\mathrm{s}}^{\mathrm{hor}}$ and maximise m through $C_{\mathrm{s}}^{\mathrm{ver-l}}$ and $C_{\mathrm{s}}^{\mathrm{ver-r}}$ and compensate by increasing the height of the inductor,
- To minimise the height of the MLAC inductor, minimise m through $C_{\mathrm{s}}^{\mathrm{ver-l}}$ and $C_{\mathrm{s}}^{\mathrm{ver-r}}$, maximise n through $C_{\mathrm{s}}^{\mathrm{hor}}$ and compensate by increasing the length of the inductor.

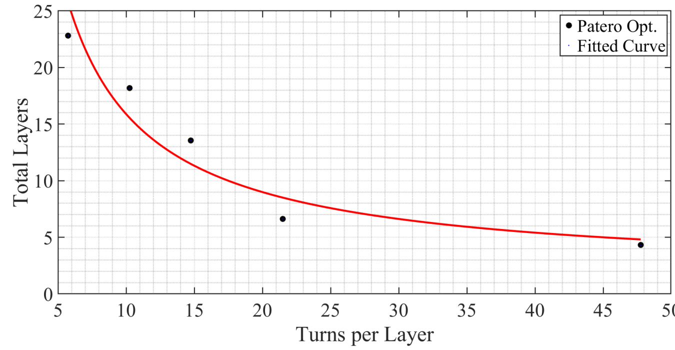

Fig. 14: Pareto Front for the Prototype Inductor C

The functions for optimisation are derived using equations in (15), (16) & (17) and are expressed as (29) (F1 for optimising m) & (30) (F2 for optimising n). For obtaining a set of solutions for POF, the first objective is the Turns per Layer (x_1) and the second objective is the Total Layers (x_2). The non-linear equality condition expressed in (31) for the inductor is from (18), (19) & (20), wherein (C_{tot}) is predefined as per the desired SRF in (22) and should be equal to the sum of the three segregated capacitances, expressed as $\mathrm{C}_{\mathrm{tot}}^{\mathrm{des}}$. Since the residues marginally contribute to the static capacitance as compared to the total segregated static capacitances, they can be ignored for the optimisation process. The expression for non-linear equality is as shown in (31), while the constraint for linear equality for POF are not considered (32). The linear constraints applied to the optimisation are :

- $C_{\mathrm{s}}^{\mathrm{hor}} \leqslant \mathrm{C}_{\mathrm{tot}}^{\mathrm{des}}$, so as to make sure the horizontal capacitance per layer does not exceed the total static capacitance,
- $C_{\mathrm{s}}^{\mathrm{ver-l}} \leqslant \mathrm{C}_{\mathrm{tot}}^{\mathrm{des}}$, so as to make sure the vertical-left capacitance per array does not exceed the total static capacitance and,
- $C_{s}^{ver-r} \leqslant \mathrm{C}_{\mathrm{tot}}^{\mathrm{des}}$, so as to make sure the vertical-right capacitance per array does not exceed the total static capacitance.
- $C_{\mathrm{s}}^{\mathrm{hor}} + C_{\mathrm{s}}^{\mathrm{ver-l}} + C_{\mathrm{s}}^{\mathrm{ver-r}} \geq \mathrm{C}_{\mathrm{tot}}^{\mathrm{des}}$, to ensure the minimum value of static capacitance is met with for a user-defined SRF.

The following linear equalities are set :

- $C_{\mathrm{s}}^{\mathrm{ver}} = C_{\mathrm{tt}}^{\mathrm{ver-l}} + C_{\mathrm{tt}}^{\mathrm{ver-l}}$, as the vertical static capacitances form exclusively over layers of the inductor,
- $C_{\mathrm{s}}^{\mathrm{hor}} = \mathrm{C}_{\mathrm{tot}}^{\mathrm{des}} - C_{\mathrm{s}}^{\mathrm{ver}}$ to maintain the conservativeness of (22)

The MLAC inductor is allowed $m = 1$ & $n = 2$ as lower bounds while $m = 100$ & $n = 100$ as upper bounds. The winding pitch for the MLAC is ideally ortho-cyclical (Fig.1b). The user-defined SRF of the MLAC is assumed linear and frequency invariant.

$$F1 = \left[\left(\frac{1}{\mathrm{C}_{\mathrm{des}}^{\mathrm{tot}}}\right)\left(\frac{C_{\mathrm{tt}}^{\mathrm{hor}}}{x_2 - 1}\right)\right] + \left[\frac{\left(C_{\mathrm{tt}}^{\mathrm{ver-l}} + C_{\mathrm{tt}}^{\mathrm{ver-r}}\right) x_1 x_2}{x_1 - 1}\right] \tag{29}$$

$$F2 = \left[\left(\frac{1}{\mathrm{C}_{\mathrm{des}}^{\mathrm{tot}}}\right)\left(\frac{C_{\mathrm{tt}}^{\mathrm{hor}} x_1 x_2}{x_2 - 1}\right)\right] + \left[\frac{\left(C_{\mathrm{tt}}^{\mathrm{ver-l}} + C_{\mathrm{tt}}^{\mathrm{ver-r}}\right)}{x_1 - 1}\right] \tag{30}$$

$$C = C_{\mathrm{tt}}\left(x_2(x_2 - 1)\right) + \frac{\left(x_1(x1 - 1)(C_{\mathrm{tt}}^{\mathrm{ver-l}} + C_{\mathrm{tt}}^{\mathrm{ver-r}})\right)}{(x_2 - 1)(x_1 - 1)} - \left(\mathrm{C}_{\mathrm{des}}^{\mathrm{tot}}\right) \tag{31}$$

$$C_{eq} = 0 \tag{32}$$

Using these objective functions, constraints, linear non-linear equalities, the POF optimisation is conducted. The inductor parameters are from laboratory prototype C, with four layers and forty-eight turns on the first layer. The user-defined first SRF is chosen as 122.55 kHz. The POF generated shows five optimal solutions (Fig.14). The POF for this inductor show that the fabricated inductor is a feasible solution. This proves that the optimisation technique can give multiple solutions for the same user-specific SRF. A polynomial curve fitting is then used to plot the decaying curve.

For any considered MLAC inductor with a pre-defined first SRF, the feasible solutions show that to maintain the static capacitance, a trade-off between the total layers and turns per layer is required. Depending on the suitability of this SRF, a feasible inductor design may be selected based on the volume requirements of the application. In addition, the set upper and lower bounds also dictate the feasible solutions, making some solutions not practically realisable. Further, the diameter of the bobbin also maybe considered as an influential parameter.

VII. Discussion

The analytical technique for the first SRF prediction in MLAC inductors has been validated experimentally using prototype inductors. The results show good agreement with the derived formulae. The observed error between the experimental verifications and analytical predictions are possibly due to the following reasons:

- The relative permittivity (ϵ_{r}) of the insulation coating is influential in calculating the first SRF. Slight variations observed due to the uneven enamel will also cause changes in the total static capacitance, especially at high frequencies, as the C_{tt} decreases from nanofarads to picofarads.
- Although the voltage between every consecutive turn on a layer is considered to be constant, it will slightly drop along the length of the inductor [30].
- The analytical approach assumes a perfect ortho-cyclical winding. This may not always be the case with the laboratory based prototype inductors as windings tend to towards wild windings as the layers are increased. Hence, the wire core's thickness along with total layers on the fabricated inductor influence the measured first SRF.
- The lumped parameter approach for the capacitive field network is limited due to the end-of-frequency effect [31] and only considered the electrostatic field and not the electromagnetic field that inherently is the resonance effect.
- The expressions ignore the fringe EFTs from the non-coupling of the turn-to-turn capacitances at the end turns of the inductor. Due to this, the accuracy of the analytical technique shall be limited within the kHz bandwidth, as the fringe EFTs become more influential in the MHz bandwidth.
- The discrepancy between the calculated and measured impedance responses for the inductor prototypes is possibly because the expressions do not consider the wire core's resistance. For deriving the impedance response, the inductance can be calculated using the Wheeler's formulae and the derived expression give the static capacitance. However, there is no method to include the resistance-per-turn of the inductors in the expression. The resulting skin-effect is also neglected in the analytical formulation.
- The development of the magnetic field is assumed to be constant, layer-by-layer in the MLAC. The EFT field is also assumed to be static between the turns and the layers of the inductor. Neglecting the dynamic changes within both these fields that lead to resonances would make for a strong assumption.
- The total mean turn length l_{T} does not remain constant, but slightly increases alongside total diameter of the inductor D_{tot}, but is assumed to be constant in the analytical derivation. An improvement or a correction in the analytical formulae may then be suggested and derived accordingly.

VIII. Conclusion

An analytical approach for predicting the first self resonance frequency in a multi-layer air core inductor using segregated electrostatic field traces has been presented. The expressions derived have been verified through laboratory based prototype inductors. The contributions of this article are as follows -

- A quick and low complexity method to compute the static capacitance of multi-layer air-core inductors to predict the first self resonance frequency is derived and verified.
- An optimisation technique for inductor design is described through multi-objective optimization using pareto-optimal fronts, that can give multiple solutions for the inductor parameters for a user-defined SRF.

The results obtained can be useful for calculating ortho-cyclically wound multi-layer air-core inductor's first self resonance to know its operational bandwidth. The optimisation procedure can help EMC engineers design inductors for a predefined self resonance and volume constraints.

Acknowledgment

This work is funded through the MSCA ETOPIA (grant agreements : 812753, 812391, 955646) at the University of Nottingham, United Kingdom and Politecnico di Milano, Italy. The practical support and guidance for the inductor fabrication & experimental verification by Matthew Cooper and the technicians at the Power Electronics and Machines Control department at the University of Nottingham is duly acknowledged.

References

[1] "CISPR/CIS/A-Radio-interference measurements and statistical methods," International Electrotechnical Commission, Geneva, CH, Standard, 2017.

[2] "Requirements for the control of the electromagnetic interferance characteristics of subsystems and equipment," International Electrotechnical Commission, Geneva, CH, Standard, 2015.

[3] M. Perry, "Multiple layer parallel connected air-core inductor design," *IEEE Transactions on Power Apparatus and Systems*, vol. PAS-98, no. 4, pp. 1387–1393, 1979. DOI: 10.1109/TPAS.1979.319341.

[4] A. J. Hanson, J. A. Belk, S. Lim, C. R. Sullivan, and D. J. Perreault, "Measurements and performance factor comparisons of magnetic materials at high frequency," *IEEE Transactions on Power Electronics*, vol. 31, no. 11, pp. 7909–7925, 2016. DOI: 10.1109/TPEL.2015.2514084.

[5] M. Solomentsev and A. J. Hanson, "At what frequencies should air-core magnetics be used?" *IEEE Transactions on Power Electronics*, vol. 38, no. 3, pp. 3546–3558, 2023. DOI: 10.1109/TPEL.2022.3222993.

[6] R. Barrera-Cardenas, T. Isobe, and M. Molinas, "Optimal design of air-core inductor for medium/high power dc-dc converters," in *2016 IEEE 17th Workshop on Control and Modeling for Power Electronics (COMPEL)*, 2016, pp. 1–8. DOI: 10.1109/COMPEL.2016.7556774.

[7] H. A. Mantooth, M. D. Glover, and P. Shepherd, "Wide bandgap technologies and their implications on miniaturizing power electronic systems," *IEEE Journal of Emerging and Selected Topics in Power Electronics*, vol. 2, no. 3, pp. 374–385, 2014. DOI: 10.1109/JESTPE.2014.2313511.

[8] B. Zhang and S. Wang, "A survey of emi research in power electronics systems with wide-bandgap semiconductor devices," *IEEE Journal of Emerging and Selected Topics in Power Electronics*, vol. 8, no. 1, pp. 626–643, 2020. DOI: 10.1109/JESTPE.2019.2953730.

[9] "Nonideal behavior of components," in *Introduction to Electromagnetic Compatibility*. John Wiley & Sons, Ltd, 2005, ch. FIVE, pp. 299–376, ISBN: 9780471758150. DOI: https://doi.org/10.1002/0471758159.ch5.

[10] C. Wm and T.McLyman, "Transformer and inductor design handbook," vol. 4th, pp. 10–1, 10–12, 2011.

[11] A. Massarini and M. Kazimierczuk, "Self-capacitance of inductors," *IEEE Transactions on Power Electronics*, vol. 12, no. 4, pp. 671–676, 1997. DOI: 10.1109/63.602562.

[12] A. Massarini, "Analytical approach to the calculation of parasitic capacitance between winding turns," in *2018 IEEE 4th International Forum on Research and Technology for Society and Industry (RTSI)*, 2018, pp. 1–4. DOI: 10.1109/RTSI.2018.8548511.

[13] G. Grandi, M. Kazimierczuk, A. Massarini, and U. Reggiani, "Stray capacitances of single-layer solenoid air-core inductors," *IEEE Transactions on Industry Applications*, vol. 35, no. 5, pp. 1162–1168, 1999. DOI: 10.1109/28.793378.

[14] A. Ayachit and M. K. Kazimierczuk, "Self-capacitance of single-layer inductors with separation between conductor turns," *IEEE Transactions on Electromagnetic Compatibility*, vol. 59, no. 5, pp. 1642–1645, 2017. DOI: 10.1109/TEMC.2017.2681578.

[15] A. Massarini, M. Kazimierczuk, and G. Grandi, "Lumped parameter models for single- and multiple-layer inductors," in *PESC Record. 27th Annual IEEE Power Electronics Specialists Conference*, vol. 1, 1996, 295–301 vol.1. DOI: 10.1109/PESC.1996.548595.

[16] A. Baccigalupi, P. Daponte, and D. Grimaldi, "On circuit theory approach to evaluate the stray capacitances of two coupled inductors," in *1993 IEEE Instrumentation and Measurement Technology Conference*, 1993, pp. 549–553. DOI: 10.1109/IMTC.1993.382582.

[17] Z. Shen, H. Wang, Y. Shen, Z. Qin, and F. Blaabjerg, "Winding design of series ac inductor for dual active bridge converters," in *2018 IEEE Applied Power Electronics Conference and Exposition (APEC)*, 2018, pp. 565–570. DOI: 10.1109/APEC.2018.8341068.

[18] ——, "An improved stray capacitance model for inductors," *IEEE Transactions on Power Electronics*, vol. 34, no. 11, pp. 11 153–11 170, 2019. DOI: 10.1109/TPEL.2019.2897787.

[19] E. Laveuve, J.-P. Keradec, and M. Bensoam, "Electrostatic of wound components: Analytical results, simulation and experimental validation of the parasitic capacitance," in *Conference Record of the 1991 IEEE Industry Applications Society Annual Meeting*, 1991, 1469–1475 vol.2. DOI: 10.1109/IAS.1991.178054.

[20] J. Collins, "An accurate method for modeling transformer winding capacitances," in *[Proceedings] IECON '90: 16th Annual Conference of IEEE Industrial Electronics Society*, 1990, 1094–1099 vol.2. DOI: 10.1109/IECON.1990.149290.

[21] X. Liu, Y. Wang, J. Zhu, Y. Guo, G. Lei, and C. Liu, "Calculation of capacitance in high-frequency transformer windings," *IEEE Transactions on Magnetics*, vol. 52, no. 7, pp. 1–4, 2016. DOI: 10.1109/TMAG.2016.2522976.

[22] H. Y. Lu, J. G. Zhu, and S. Hui, "Experimental determination of stray capacitances in high frequency transformers," *IEEE Transactions on Power Electronics*, vol. 18, no. 5, pp. 1105–1112, 2003. DOI: 10.1109/TPEL.2003.816186.

[23] G. Grandi, U. Reggiani, and M. Kazimierczuk, "Optimal design of single-layer solenoid air-core inductors for high frequency applications," in *Proceedings of 40th Midwest Symposium on Circuits and Systems. Dedicated to the Memory of Professor Mac Van Valkenburg*, IEEE, vol. 1, 1997, pp. 358–361.

[24] D. K. Saini, A. Ayachit, and M. K. Kazimierczuk, "Design and characterisation of single-layer solenoid air-core inductors," *IET Circuits, Devices & Systems*, vol. 13, no. 2, pp. 211–218, 2019. DOI: 10.1049/iet-cds.2018.5082.

[25] L. F. de Freitas Gutierres and G. Cardoso, "Analytical technique for evaluating stray capacitances in multiconductor systems: Single-layer air-core inductors," *IEEE Transactions on Power Electronics*, vol. 33, no. 7, pp. 6147–6158, 2018. DOI: 10.1109/TPEL.2017.2745213.

[26] C. W. T. McLyman, "Transformer and inductor design handbook," 2011.

[27] N. B. Chagas and T. B. Marchesan, "Analytical calculation of static capacitance for high-frequency inductors and transformers," *IEEE Transactions on Power Electronics*, vol. 34, no. 2, pp. 1672–1682, 2019. DOI: 10.1109/TPEL.2018.2829716.

[28] X. Wang, H. Zeng, D. Gunasekaran, and F. Z. Peng, "Multi-objective design and optimization of inductors: A generalized software-driven approach," in *2016 IEEE 17th Workshop on Control and Modeling for Power Electronics (COMPEL)*, 2016, pp. 1–7. DOI: 10.1109/COMPEL.2016.7556750.

[29] R. González-Echevarría, E. Roca, R. Castro-López, *et al.*, "An automated design methodology of rf circuits by using pareto-optimal fronts of em-simulated inductors," *IEEE Transactions on Computer-Aided Design of Integrated Circuits and Systems*, vol. 36, no. 1, pp. 15–26, 2017. DOI: 10.1109/TCAD.2016.2564362.

[30] L. Wan, A. D. Khilnani, X. Wu, *et al.*, "Optimal design of single-layer and multi-layer air-core inductors considering uncertainty factors," *IEEE Access*, vol. 11, pp. 134 460–134 472, 2023. DOI: 10.1109/ACCESS.2023.3336572.

[31] H. Zhao, S. Luan, Z. Shen, *et al.*, "Rethinking basic assumptions for modeling parasitic capacitance in inductors," *IEEE Transactions on Power Electronics*, vol. 37, no. 7, pp. 8281–8289, 2022. DOI: 10.1109/TPEL.2021.3139682.

Arun Dilip Khilnani (SM'–19) received his master's degree in Electric Power Engineering from Chalmers University of Technology, Sweden, in 2019, and the bachelor's degree in Electrical Engineering from the University of Mumbai, India, in 2009. Since October 2019, he is working towards the Ph.D. degree at the University of Nottingham in the Department of Electrical and Electronic Engineering. His research interests are focused on Electromagnetic Compatibility and Power Electronics.

Lu Wan (SM'–19, M'–23) received the double M.Sc. degree in Electrical Engineering from Xi'an Jiaotong University, Xi'an, China, and Politecnico di Milano, Milan, Italy, in 2017, and the joint Ph.D. degree (summa cum laude) in Electrical Engineering from Politecnico di Milano and the University of Craiova in 2023. From 2017 to 2019, he was an Assistant Researcher at the Electric Power Research Institute, China Southern Power Grid. He is currently a Postdoctoral Researcher at the Energy Department, Aalborg University. His research interests include electromagnetic interference of power converters, EMI mitigation, filter design, and experimental procedures.

Danny Robert Seeley (SM'–19) MEng (Hons), MIEEE, graduated from the University of Nottingham in 2020 with an MEng in Electrical and Electronic Engineering, specializing in Digital Signal Processing. He is currently completing a PhD in DC power system protection with the Power Electronics, Machines and Control group at the University of Nottingham. His other research interests include arc fault generation, fault location, and studying the impacts of changing environmental conditions on reliable power system protection.

Mark Sumner (Senior Member, IEEE) received the B.Eng. degree in electrical and electronic engineering from the University of Leeds in 1986, and the Ph.D. degree in induction motor drives from the University of Nottingham, U.K., in 1990. He was with Rolls Royce Ltd., U.K. He was also a Research Assistant and a Lecturer in October 1992. He is currently a Professor of Electrical Energy Systems with the Power Electronics, Machines and Control Group, University of Nottingham. His research interests include control of power electronic systems, including sensorless motor drives, diagnostics and prognostics for drive systems, power electronics for enhanced power quality, and novel power system fault location strategies.

Dave Thomas (Senior Member, IEEE) received the B.Sc. degree in physics from Imperial College, London, U.K., in 1981, the M.Phil. degree in space physics from Sheffield University, Sheffield, U.K., in 1984, and the Ph.D. degree in electrical engineering from Nottingham University, Nottingham, U.K., in 1990. He is a Professor of electromagnetics applications with the George Green Institute for Electromagnetics Research, The University of Nottingham, Nottingham, UK. He is a member of CIGRE and Convenor for Joint Working Group C4.31 EMC between communication circuits and power systems, Chair of COST Action IC 1407 'Advanced characterisation and classification of radiated emissions in densely integrated technologies', a member of several conference committees, and the EMC Europe International Steering Committee. His research interests include electromagnetic compatibility, electromagnetic simulation, power system transients, and power system protection.

Flavia Grassi (Senior Member, IEEE) received the laurea (M.Sc.) and Ph.D. degrees in electrical engineering from Politecnico di Milano, Milan, Italy, in 2002 and 2006, respectively. She is currently a Full Professor with the Department of Electronics, Information and Bioengineering, Politecnico di Milano. From 2008 to 2009, she was with the European Space Agency (ESA), ESA/ESTEC, The Netherlands, as a Research Fellow. Her research interests include: Theoretical and experimental characterization of EM interference via lumped and distributed circuit modeling; characterization and development of measurement procedures and setups for EMC assessment of avionic, automotive, and power systems; statistical techniques, EMC and coexistence issues in power systems. Dr. Grassi received the International Union of Radio Science Young Scientist Award in 2008, and the IEEE Young Scientist Award at the 2016 Asia-Pacific International Symposium on EMC, the IEEE EMC Society 2016 and 2021 Transactions Prize Paper Award, and the Best Symposium Paper Award at the 2015 and 2018 APEMC.